Wave propagation in random 2D turbulence: a multi-scale approach

Valentin Resseguier, Erwan Hascoët, Bertrand Chapron

Wave propagation in random 2D turbulence: a multi-scale approach

Valentin Resseguier[1,2] †, Erwan Hascoët[3] and Bertrand Chapron[4]

[1]ACTA, OPAALE, INRAE

[2]Lab, SCALIAN DS

[3]Oceandatalab

[4]LOPS, Ifremer

(Received xx; revised xx; accepted xx)

To study two-dimensional dispersive waves propagating over turbulent flows, a new and less restrictive fast waves approximation is proposed using a multiscale setting. In this ansatz, correlation lengths of the random small scale turbulence components can be considered negligible in the wave packet propagating frame. Still, the large-scale flow can be relatively strong, to significantly impact wavenumbers along the propagating rays. New theoretical results, numerical tools and proxies are derived to describe ray and wave action distributions. All model parameters can robustly be calibrated from the large-scale flow component only. We illustrate our purpose with ocean surface gravity waves propagating in different types of surface currents. The multiscale solution is demonstrated to efficiently document wave trapping effects by intense jets.

Key words:

MSC Codes 76B15,76M35, 82B31,82C31, 37H10, 37L55

1. Introduction

This paper aims to revisit the ray-path concept for fast waves propagating over heterogeneous turbulent flows. Considering ocean surface wave propagation, many authors have already discussed the random changes of rays subject to a random current (Voronovich 1991; White & Fornberg 1998; Smit & Janssen 2019), and consequences on wave action distributions. Closures have been derived in the Eulerian setting (Bal & Chou 2002; Klyatskin & Koshel 2015; Borcea *et al.* 2019; Kafiabad *et al.* 2019; Bôas & Young 2020; Garnier *et al.* 2020). Some of these approaches can be traced back to wave-wave interactions models, e.g. McComas & Bretherton (1977) (see also Kafiabad *et al.* 2019, and reference therein). In most cases, the central assumption is either delta-correlated turbulence (Voronovich 1976; Klyatskin 2005; Klyatskin & Koshel 2015) and/or fast waves in comparison to fluid flow

† Email address for correspondence: valentin.resseguier@inrae.fr

velocities (White & Fornberg 1998; Dysthe 2001; Bal & Chou 2002; Borcea *et al.* 2019; Kafiabad *et al.* 2019; Smit & Janssen 2019; Bôas & Young 2020; Garnier *et al.* 2020; Boury *et al.* 2023; Wang *et al.* 2023). Medium variations may be slow and delta-correlations are hardly justifiable in a fixed frame. Though, attached to a fast propagating wave group, the medium may seem to vary rapidly, and the delta-correlation assumption makes more sense. Another common assumption is frozen turbulence. In such a case, weak currents also implies conservation along ray of intrinsic frequency, wavenumber, and group velocity magnitude in two dimension (Boury *et al.* 2023). Subsequently, most of wave dynamics closures neglect variations and diffusion of frequency or wavenumber.

The diffusion of the wave action at large distance with a multiscale decomposition of the current has already been reported Bal & Chou (2002). However, an explicit formulation for the diffusivity has solely been derived for a zero large-scale current. More generally, fast wave models mostly rely either on zero or constant current components at larger scales. West (1978), for instance, discussed acoustic waves in a two-component random media, but no velocity was involved.

Hereafter, the proposed two-scale velocity decomposition falls into the family of stochastic transport models (Kunita 1997; Mikulevicius & Rozovskii 2004; Resseguier *et al.* 2020*a*; Zhen *et al.* 2023), including dynamics under Location Uncertainty (LU) (Mémin 2014; Resseguier *et al.* 2017*a*) and Stochastic Advection by Lie Transport (SALT) (Holm 2015). Under this framework, resulting conservative stochastic closures build on time delta-correlation for the small-scale turbulence component (Cotter *et al.* 2017). Nonlinear wave Hamiltonian dynamics and wave influence on currents (e.g. stokes drift) have then been derived (e.g. Crisan & Holm 2018; Bauer *et al.* 2020; Holm 2021; Holm & Luesink 2021; Dinvay & Mémin 2022; Holm *et al.* 2023). Considering a single-wavevector current, solutions for a monochromatic shallow water wave were developed Mémin *et al.* (2022). In the present study, our objective is restricted to the influence of turbulent flows on linear waves.

After first recalling the principle of ray tracing method, we present the multiscale framework for fast waves dynamics, its physical ground and a calibration method for the closure. Simplified stochastic equations are then derived for ray dynamics and wave action spectrum, in both Lagrangian and Eulerian settings. For illustrative examples, numerical tools, analytic models and proxies are applied to ocean surface gravity waves propagating through two types of 2D turbulent flows: a typical slow homogeneous turbulence and a jet case.

2. Characteristics of wave-packet rays

Isolating a single progressive group of quasi-regular wave train, it follows a form $h(\boldsymbol{x},t)e^{\mathrm{i}\phi(\boldsymbol{x},t)}$ + c.c., for most properties. If a packet is to be followed, the phase, $\phi(\boldsymbol{x},t)$, must smoothly vary along the propagation, i.e. $\phi(\boldsymbol{x},t)$ is differentiable. The relative frequency is then $\omega = -\partial_t\phi(\boldsymbol{x},t)$, and the wave number vector $\boldsymbol{k} = \boldsymbol{\nabla}\phi(\boldsymbol{x},t)$, with wavenumber $k = \|\boldsymbol{k}\|$ and direction given by the normalized wave-vector, $\tilde{\boldsymbol{k}} = \boldsymbol{k}/k = \begin{pmatrix}\cos\theta_k\\ \sin\theta_k\end{pmatrix}$. To first order, such a train of waves is dispersive and the intrinsic frequency reads

$$\omega - \boldsymbol{k}\cdot\boldsymbol{v} = \omega_0 = \begin{cases}\text{cst.}\,\frac{1}{\alpha}k^{\alpha}, & \alpha \neq 0\\ \text{cst.}\,\log(k), & \alpha = 0\end{cases} \tag{2.1}$$

and propagates with its group velocity $\boldsymbol{v}_g = \boldsymbol{\nabla}_{\boldsymbol{k}}\omega$, constantly modified by the local velocity of the currents $\boldsymbol{v}$,

$$\frac{\mathrm{d}\boldsymbol{x}_r}{\mathrm{d}t} = \boldsymbol{v}_g = \boldsymbol{v}_g^0 + \boldsymbol{v}, \tag{2.2}$$

where $\boldsymbol{x}_r$ is the centroid of a wave group, $\boldsymbol{v}_g^0 = \frac{\partial\omega_0(k)}{\partial k}\tilde{\boldsymbol{k}}$ is the group velocity without currents, i.e. solely depending on the wave vector. For $\alpha = 1$, the medium is non-dispersive (e.g. acoustic waves). $\alpha = 1/2$ corresponds to gravity waves over deep ocean ($\omega_0 = \sqrt{gk}$). The dominant wave-vector $\boldsymbol{k}$ within the group evolves according to

$$\frac{\mathrm{d}\boldsymbol{k}}{\mathrm{d}t} = -\boldsymbol{\nabla}\boldsymbol{v}^{\mathsf{T}}\boldsymbol{k}. \tag{2.3}$$

Equations (2.2)-(2.3) are the Hamilton' s eikonal equations. Along the propagating ray, velocity gradients induce linear variations. Decelerating currents will, for instance, shorten waves, and reduce the group velocity. Traveling over fields of random velocities $\boldsymbol{v}$, the wave-vector $\boldsymbol{k}$ will also become randomly distributed. Scattering of ocean surface wave packets by random currents can generally be assumed to be weak, with $\|\boldsymbol{v}\|$ of order 0.5 $\mathrm{m.s}^{-1}$, much smaller than $v_g^0 = \|\boldsymbol{v}_g^0\|$ of order 10 $\mathrm{m.s}^{-1}$. Yet, cumulative effects of these random surface currents can lead to strong convergence or divergence between initially nearby ray trajectories.

To complete the wave field description, the wave action, $A(\boldsymbol{x},t) = h^2(\boldsymbol{x},t)/\omega_0(k(\boldsymbol{x},t))$, is considered to be an adiabatic invariant in absence of source terms. Wave action is then crucial to anticipate wave transformations by currents (White 1999). Unlike wave energy, wave action is conserved, in the absence of wave generation or dissipation. This action is the integral over wave-vectors of the action spectrum, N, also related to the wave energy spectrum, E:

$$A(\boldsymbol{x},t) = \int \mathrm{d}\boldsymbol{k}\; N(\boldsymbol{x},\boldsymbol{k},t) = \int \mathrm{d}\boldsymbol{k}\; \frac{E(\boldsymbol{x},\boldsymbol{k},t)}{\omega_0(k,t)}. \tag{2.4}$$

Action and energy spectrum quantify action and energy by unit of surface (unit of $\boldsymbol{x}$) and by unit of wave-vector surface (unit of $\boldsymbol{k}$). Consider the $(\boldsymbol{x},\boldsymbol{k})$ variable change between different times t_i and t_f integrating the characteristic eikonal equations (2.2)-(2.3)

$$\begin{pmatrix}\boldsymbol{x}_r(t_i)\\ \boldsymbol{k}(t_i)\end{pmatrix} \mapsto \begin{pmatrix}\boldsymbol{x}_r(t_f)\\ \boldsymbol{k}(t_f)\end{pmatrix} \tag{2.5}$$

By the Liouville theorem and since $\boldsymbol{\nabla}_{\boldsymbol{x}}\cdot\frac{\mathrm{d}\boldsymbol{x}_r}{\mathrm{d}t} + \boldsymbol{\nabla}_{\boldsymbol{k}}\cdot\frac{\mathrm{d}\boldsymbol{k}}{\mathrm{d}t} = 0$, the state-space of the "packet-by-packet" approach (the $(\boldsymbol{x},\boldsymbol{k})$ space) does not contract nor dilates along time. Therefore, if wave dissipation is neglected, the wave action spectrum N is conserved Lavrenov (2013), i.e.

$$N\left(\boldsymbol{x}_r(t_i),\boldsymbol{k}(t_i),t_i\right) = N\left(\boldsymbol{x}_r(t_f),\boldsymbol{k}(t_f),t_f\right). \tag{2.6}$$

This result is extremely useful because it only involves quantities of the characteristics, i.e. each Fourier mode can be modified independently of the others. The wave energy spectrum can be computed from the characteristics

$$E\left(\boldsymbol{x}_r(t_f),\boldsymbol{k}(t_f),t_f\right) = \frac{\omega_0(\boldsymbol{k}(t_f))}{\omega_0(\boldsymbol{k}(t_i))}\, E\left(\boldsymbol{x}_r(t_i),\boldsymbol{k}(t_i),t_i\right). \tag{2.7}$$

starting with an initial incoming wave spectrum $E\left(\boldsymbol{x}_r(t_i),\boldsymbol{k}(t_i),t_i\right)$ for every wave-vectors $\boldsymbol{k}(t_i)$, starting from a small set of spatial points $\boldsymbol{x}_r(t_i)$.

3. A new fast wave assumption

Commonly, the Eulerian current $\boldsymbol{v}$ is decomposed into a low-frequency large-scale component $\overline{\boldsymbol{v}}$ and a transient small-scale unresolved component $\boldsymbol{v}'$:

$$\boldsymbol{v} = \overline{\boldsymbol{v}} + \boldsymbol{v}'. \tag{3.1}$$

From now, we shall consider divergence-free two-dimensional currents only.

3.1. *The ray Lagrangian correlation time*

To better characterize the wave dynamics in such a random environment, the covariance of the fluid velocity can be evaluated in the wave group frame. To take into account the small-scale unresolved component $\boldsymbol{v}'$, its Eulerian spatio-temporal covariance is considered, assuming statistical homogeneity and stationarity for the Eulerian velocity $\boldsymbol{v}'_E(t,\boldsymbol{x}) = \boldsymbol{v}'(t,\boldsymbol{x})$

$$C_{ij}^{v'_E}(\delta t, \delta \boldsymbol{x}) = \mathbb{E}\left(v'_i(t,\boldsymbol{x})v'_j(t+\delta t, \boldsymbol{x}+\delta\boldsymbol{x})\right) = \mathbb{E}\left(v'_i(t,\boldsymbol{x}_r(t))v'_j(t+\delta t, \boldsymbol{x}_r(t)+\delta\boldsymbol{x})\right) \tag{3.2}$$

where $\boldsymbol{x}_r$ is solution of (2.2) with an arbitrary initial position $\boldsymbol{x}_r^0$. Then, we define, $v'_R(t) = v'(t,\boldsymbol{x}_r(t))$, the Lagrangian velocity along the ray $\boldsymbol{x}_r(t)$. The temporal covariance of the small-scale component $\boldsymbol{v}'$ – in the wave group frame – is the covariance of that Lagrangian velocity:

$$C_{ij}^{v'_R}(\delta t) = \mathbb{E}\left(v'_i(t,\boldsymbol{x}_r(t))v'_j(t+\delta t, \boldsymbol{x}_r(t+\delta t))\right) = C_{ij}^{v'_E}(\delta t, \boldsymbol{x}_r(t+\delta t) - \boldsymbol{x}_r(t)), \tag{3.3}$$

Assume a typical isotropic form for this covariance:

$$C^{v'_E}(\delta t, \delta\boldsymbol{x}) = C\left(\frac{|\delta t|}{\tau_{v'}} + \frac{\|\delta\boldsymbol{x}\|}{l_{v'}}\right), \tag{3.4}$$

the covariance can be evaluated in the wave group frame for small time increment δt:

$$C^{v'_R}(\delta t) = C\left(\frac{|\delta t|}{\tau_{v'}} + \frac{\|\boldsymbol{x}_r(t'+t) - \boldsymbol{x}_r(t')\|}{l_{v'}}\right) = C\left(\left(\frac{1}{\tau_{v'}} + \frac{\|\boldsymbol{v}_g\|}{l_{v'}}\right)|\delta t| + O(\delta t^2)\right). \tag{3.5}$$

Therefore, $\left(\frac{1}{\tau_{v'}} + \frac{\|\boldsymbol{v}_g\|}{l_{v'}}\right)^{-1}$ is the correlation time of $\boldsymbol{v}'(t,\boldsymbol{x}_r(t))$. The same derivation is valid for $\boldsymbol{\nabla}(\boldsymbol{v}')^{\mathsf{T}}(t,\boldsymbol{x}_r(t))$. For fast waves, the along-ray correlation time of the small-scale velocity can be approximated by $l_{v'}/v_g^0$. The ratio ϵ, between this along-ray correlation time and the characteristic time of the wave group properties evolution, will then control the time decorrelation assumption of $\boldsymbol{v}'$:

$$\epsilon = \frac{l_{v'}}{v_g^0}\|\boldsymbol{\nabla}\boldsymbol{v}^{\mathsf{T}}\| \sim \frac{l_{v'}}{l_v}\frac{\|\boldsymbol{v}\|}{v_g^0}. \tag{3.6}$$

Note the Eulerian small-scale velocity $\boldsymbol{v}'$ is not necessarily time uncorrelated, as assumed in Voronovich (1976); Klyatskin & Koshel (2015). Yet, for small enough ϵ, the Lagrangian small-scale velocity along the ray can be considered time uncorrelated. From the expression of ϵ, such a condition depends upon:

- v_g^0, the fast wave group velocity
- $\|\boldsymbol{v}\|$, often slow but not always negligible compared to the intrinsic wave group, v_g^0.
- $l_{v'}/l_v$, related to the separation between large scales $\overline{\boldsymbol{v}}$ and small scales $\boldsymbol{v}'$, e.g. the spatial filtering cutoff of the large-scale velocity $\overline{\boldsymbol{v}}$, but also related to its kinetic energy (KE) distribution over spatial scales, typically the spectrum slope.

This along-ray partially time-decorrelation assumption is less restrictive than the usual fast wave approximation (White & Fornberg 1998; Dysthe 2001; Bal & Chou 2002; Borcea *et al.* 2019; Kafiabad *et al.* 2019; Smit & Janssen 2019; Bôas & Young 2020; Garnier *et al.* 2020; Boury *et al.* 2023; Wang *et al.* 2023) – say $\frac{\|\boldsymbol{v}\|}{v_g^0} \ll 1$ – and than the SALT-LU time-decorrelation used for turbulence dynamics (Mémin 2014; Holm 2015; Cotter *et al.* 2017; Resseguier *et al.* 2020*a*) – say $\frac{l_{v'}}{l_v} \ll 1$. Similarly, this last validity criterion can be obtained replacing in (3.2)-(3.6) $\boldsymbol{x}_r$ by the fluid particle Lagrangian path $\boldsymbol{x}$ (solution of $\frac{\mathrm{d}\boldsymbol{x}}{\mathrm{d}t} = \boldsymbol{v}$) and thus $\boldsymbol{v}_g^0$ by $\boldsymbol{v}$. These asymptotic models often rely on averaging or homogenization techniques (Papanicolaou & Kohler 1974; White & Fornberg 1998) to derive Markovian dynamics involving various types of diffusivity.

3.2. *Ray absolute diffusivity and turbulence statistics: calibration*

Diffusivity is a natural tool to specify statistics of uncorrelated random media. For waves in random media, we shall specify multi-point statistics, and the Fourier space is convenient for this purpose. We will first present scalar diffusivity and then distribute it over spatial scales to fully calibrate the random velocity $\boldsymbol{v}'$.

The absolute diffusivity (or Kubo-type formula) usually corresponds, in the so-called diffusive regime, to the variance per unit of time of a fluid particle Lagrangian path $\frac{\mathrm{d}\boldsymbol{x}(t)}{\mathrm{d}t} = \boldsymbol{v}_L(t) = \boldsymbol{v}(t, \boldsymbol{x}(t))$. It is approximately equal to the velocity variance times its correlation time. The Eulerian velocity covariance (3.4) will thus induce an absolute diffusivity (Piterbarg & Ostrovskii 1997; Klyatskin 2005)

$$\tfrac{1}{2}a^L = \int_0^\infty \mathrm{d}\delta t\; C^{v'_L}(\delta t) = \int_0^\infty \mathrm{d}\delta t\; C^{v'_E}(\delta t, \boldsymbol{x}(t+\delta t) - \boldsymbol{x}(t)) \approx \tfrac{1}{2}\tau_{v'}\; C(0). \tag{3.7}$$

Along a propagating wave group, a ray absolute diffusivity occurs and slightly differs from the usual absolute diffusivity to become

$$\tfrac{1}{2}a^R = \int_0^\infty \mathrm{d}\delta t\; C^{v'_R}(\delta t) \approx \tfrac{1}{2}\left(\frac{1}{\tau_{v'}} + \frac{\|\boldsymbol{v}_g\|}{l_{v'}}\right)^{-1} C(0) \approx \tfrac{1}{2}\frac{l_{v'}}{v_g^0}\; C(0). \tag{3.8}$$

The absolute diffusivity sets the amplitude of the small scale velocity $\boldsymbol{v}'$. To calibrate its spatial correlations, we may focus on its Fourier transform, $\widehat{\boldsymbol{v}'}(\boldsymbol{\kappa}, t)$, denoting by $\boldsymbol{\kappa} = \kappa\begin{pmatrix}\cos\theta_\kappa \\ \sin\theta_\kappa\end{pmatrix}$, the surface current wave-vector. By analogy with the current kinetic energy spectra $E_\kappa = \frac{1}{2}\oint_0^{2\pi} \mathrm{d}\theta_\kappa \kappa \frac{\|\widehat{\boldsymbol{v}}(\boldsymbol{\kappa},t)\|^2}{(2\pi)^2}$, Resseguier *et al.* (2017*b*, 2020*b*) decompose the absolute diffusivity scale by scale. Referring it to Absolute Diffusivity Spectral Density (ADSD), they defined it by

$$\tfrac{1}{2}A^R(\kappa) = \tfrac{1}{2}\frac{1/\kappa}{v_g^0(k)}\; E_k(\kappa), \tag{3.9}$$

where k denotes the wave wavenumber and κ the current wavenumber. To calibrate an equivalent noise, we model $\boldsymbol{v}'$ by $\sigma \mathrm{d}B_t/\mathrm{d}t$, where $\mathrm{d}B_t/\mathrm{d}t$ is a spatio-temporal white noise and σ denotes a spatial filtering operator which encodes spatial correlations through $A^R_{v'}$ and the horizontal incompressibility condition ($\boldsymbol{\nabla}\cdot\sigma = 0$). Specifically, we assume an ADSD power law, $A^R(\kappa) \approx A_0^R \kappa^{-\mu}$, and we choose a divergence-free isotropic spatial filter $\boldsymbol{\nabla}^\perp\breve{\psi}_\sigma$ such that

$$\boldsymbol{v}' = \sigma \mathrm{d}B_t/\mathrm{d}t = \boldsymbol{\nabla}^\perp\breve{\psi}_\sigma \star \mathrm{d}B_t/\mathrm{d}t, \tag{3.10}$$

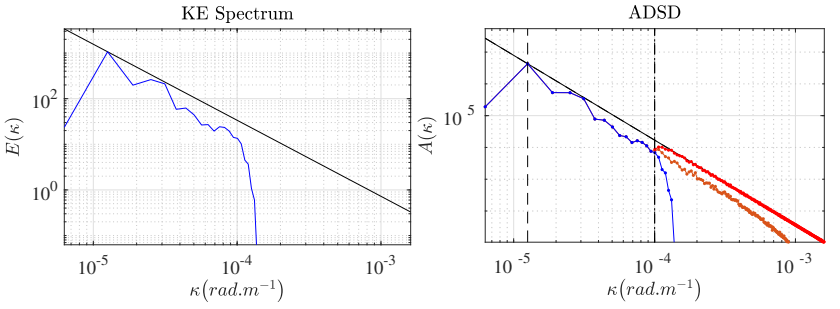

Figure 1: KE spectrum ($m^2.s^{-2}/(\mathrm{rad}.m^{-1})$) (left) and ADSD ($m^2.s^{-1}/(\mathrm{rad}.m^{-1})$) (right) of the resolved high-resolution velocity, A^R, in brown, low-resolution velocity, $A^R_{\overline{v}}$, in blue, and modeled stochastic velocity, $A^R_{v'}(\kappa) = A^R_0\kappa^{-\mu} - A^R_{\overline{v}}(\kappa)$, in red. For the ADSD power law, $A^R(\kappa) \approx A^R_0\kappa^{-\mu}$, we impose the theoretical KE spectrum slope $-\frac{5}{3}$ (black solid line), coherently with homogeneous SQG dynamics (see "Numerical results" section). The residual ADSD (red line) is set to extrapolate that power law at small scales.

and $\frac{\partial \mathrm{i}\kappa^3}{(2\pi)^2}|\widehat{\breve{\psi}_\sigma}(\kappa)|^2 = \frac{1}{2}\oint_0^{2\pi}\mathrm{d}\theta_\kappa\kappa\frac{\|\widehat{\sigma\mathrm{d}B_t}(\kappa)\|^2}{(2\pi)^2\mathrm{d}t} = A^R_{v'}(\kappa)$. The power law assumption enables automatic closure calibration: $A^R_{v'}(\kappa) = A^R_0\kappa^{-\mu} - A^R_{\overline{v}}(\kappa)$, from instantaneous large-scale current statistics $A^R_{\overline{v}}$ only (Resseguier *et al.* 2020*b*) as illustrated in figure 1.

4. Statistical wave dynamics

In a stochastic framework, the Stratonovich or Itō notations can both be used (Kunita 1997; Oksendal 1998). Under Stratonovich calculus rules, expressions become similar to deterministic ones. Specifically, stochastic versions of linearized dynamical equations are obtained by replacing $\boldsymbol{v}$ by $\overline{\boldsymbol{v}} + \sigma \circ \mathrm{d}B_t/\mathrm{d}t$. Then, the stochastic transport of phase, $\frac{\mathrm{d}}{\mathrm{d}t}\phi = \omega_0(\|\boldsymbol{\nabla}\phi\|)$, i.e. – up to that velocity replacement – the Stratonovich dispersion relation is exactly (2.1). The method of characteristics also applies. Note, one can switch from Stratonovich to Itō notations, where $\boldsymbol{v}'$ corresponds to $\sigma\mathrm{d}B_t/\mathrm{d}t$. The characteristics equations (2.2)-(2.3) also remain unchanged for homogeneous and isotropic $\boldsymbol{v}'$:

$$\begin{cases} \mathrm{d}\boldsymbol{x}_r = (\boldsymbol{v}_g^0 + \overline{\boldsymbol{v}})\mathrm{d}t + \sigma\mathrm{d}B_t, \\ \mathrm{d}\boldsymbol{k} = -\boldsymbol{\nabla}(\overline{\boldsymbol{v}}\mathrm{d}t + \sigma\mathrm{d}B_t)^\mathsf{T}\boldsymbol{k}. \end{cases} \tag{4.1}$$

4.1. *Single-ray stochastic differential equations*

When studying a single ray in an homogeneous and isotropic turbulence (3.10), the wave-vector dynamics simplifies. In the local crest-oriented frame, the influence of small scale currents can be solely represented by four one-dimensional white noise forcings.

Notably, dynamics of wave-vectors (2.3) are similar to tracer gradient dynamics (Bühler 2009; Plougonven & Zhang 2014). Only the coupled ray path dynamics (2.2) differs. Accordingly, we follow the notations and derivations of the mixing analysis from Lapeyre *et al.* (1999) and references therein. Without loss of generality, the large-scale velocity can be parameterized as

$$\overline{\boldsymbol{v}} = \overline{v}\begin{pmatrix}\cos\overline{\theta}\\ \sin\overline{\theta}\end{pmatrix} \quad \text{and} \quad \boldsymbol{\nabla}\overline{\boldsymbol{v}}^\mathsf{T} = \frac{1}{2}\begin{bmatrix}\overline{\sigma}\sin 2\overline{\phi} & \overline{\omega} + \overline{\sigma}\cos 2\overline{\phi}\\ -\overline{\omega} + \overline{\sigma}\cos 2\overline{\phi} & -\overline{\sigma}\sin 2\overline{\phi}\end{bmatrix}. \tag{4.2}$$

The influence of the large-scale currents on the ray dynamics (4.1), expressed in the local crest-oriented frame $(\tilde{\boldsymbol{k}}, \tilde{\boldsymbol{k}}^\perp)$, is straightforward (Lapeyre *et al.* 1999). The small-scale

currents force the ray dynamics through a stochastic noise. For a single ray $(\boldsymbol{x}_r, \boldsymbol{k}) = (x_r, y_r, k\cos\theta_k, k\sin\theta_k)$, this noise can be rigorously described by four independent one-dimensional white noises only (see Appendix), $\dot{B}_t^{(1)}$, $\dot{B}_t^{(2)}$, $\dot{B}_t^{(3)}$, and $\dot{B}_t^{(4)}$, and:

$$\frac{\mathrm{d}}{\mathrm{d}t}x_r = v_g^0\cos\theta_k + \overline{v}\cos\overline{\theta} + \sqrt{a_0}\dot{B}_t^{(1)}, \tag{4.3}$$

$$\frac{\mathrm{d}}{\mathrm{d}t}y_r = v_g^0\sin\theta_k + \overline{v}\sin\overline{\theta} + \sqrt{a_0}\dot{B}_t^{(2)}, \tag{4.4}$$

$$\frac{\mathrm{d}}{\mathrm{d}t}\log k = -\overline{\sigma}\sin(\zeta) + \gamma_0 + \sqrt{\gamma_0}\dot{B}_t^{(3)}, \tag{4.5}$$

$$\frac{\mathrm{d}}{\mathrm{d}t}\theta_k = \tfrac{1}{2}(\overline{\omega} - \overline{\sigma}\cos(\zeta)) + \sqrt{3\gamma_0}\dot{B}_t^{(4)}, \tag{4.6}$$

where $\zeta = 2(\theta_k + \overline{\phi})$ and

$$a_0 = \tfrac{1}{2\mathrm{d}t}\mathbb{E}\|\sigma\mathrm{d}B_t\|^2 = \int_0^{+\infty} A_{v'}^R(k)\mathrm{d}k, \tag{4.7}$$

$$\gamma_0 = \tfrac{1}{8\mathrm{d}t}\mathbb{E}\|\boldsymbol{\nabla}_{\boldsymbol{x}}(\sigma\mathrm{d}B_t)^{\mathsf{T}}\|^2 = \tfrac{1}{4}\int_0^{+\infty} k^2 A_{v'}^R(k)\mathrm{d}k \tag{4.8}$$

Diffusivity constants depend through (3.9) on both the correlation length and the spectrum slope of the small-scale velocity. Contrasting the classical fast wave approximation, the wavenumber does vary. This is due to (i) the finite large-scale strain rate, $\overline{\sigma}$, and (ii) the small-scale isotropic velocity model (3.10). This isotropy assumption and its implication are discussed in Appendix. Note that neither large-scale nor small-scale component is assumed to be steady, even though the small-scale time variations are mainly driven by the wave speed and not by their Eulerian correlation time. The current unsteadiness can also lead to wavenumber variations (Dong *et al.* 2020; Cox *et al.* 2023; Boury *et al.* 2023). Given a known wavevector angle, it leads to a wavenumber evolution

$$k(t) = k(0)\exp\left(-\int_0^t \overline{\sigma}\sin(2(\theta_k + \overline{\phi}))\right)\exp\left(\gamma_0 t + \sqrt{\gamma_0}B_t^{(3)}\right), \tag{4.9}$$

and hence the complete wavevector distribution, i.e. the wave spectrum. The second exponential factor in (4.9) is a geometric Brownian motion. Its mean diverges in time exponentially rapidly. Physically, shear and strain of $\boldsymbol{v}'$ tends to shorten the wavelength (Voronovich 1991; Boury *et al.* 2023) leading to this divergence. This factor has a log-normal distribution, suggesting possible extreme transient wavenumber events. This generalizes previous results Voronovich (1991); Klyatskin & Koshel (2015), obtained with neglecting the time-correlated current component, $\overline{\boldsymbol{v}}$.

For completeness, the action distribution over space and wave vector can be derived. Some approaches consider finite-size wave trains either through additional equations (Jonsson 1990; White & Fornberg 1998) or re-meshing (Hell *et al.* in preparation). Otherwise, each ray transports its action spectrum (2.6) and we need to numerically combine many rays (Lavrenov 2013), or rely on analytic approximations. Typically, we solve (4.3)-(4.5) exhibiting, $p(\boldsymbol{x}, \boldsymbol{k}|\boldsymbol{x}_r^0, \boldsymbol{k}_r^0, t)$, the distribution of the ray $(\boldsymbol{x}, \boldsymbol{k})$ at time t given initial conditions $(\boldsymbol{x}_r^0, \boldsymbol{k}^0)$. Then, by analogy with tracers in incompressible turbulence (Piterbarg & Ostrovskii 1997, equation (1.31)) we can evaluate the wave action spectrum mean – or any point-wise statistics – as follows

$$\mathbb{E}N(\boldsymbol{x}, \boldsymbol{k}, t) = \iint \mathrm{d}\boldsymbol{x}_r^0\mathrm{d}\boldsymbol{k}^0\; N^0(\boldsymbol{x}_r^0, \boldsymbol{k}_r^0)p(\boldsymbol{x}, \boldsymbol{k}|\boldsymbol{x}_r^0, \boldsymbol{k}^0, t) \tag{4.10}$$

where N^0 is the initial wave action spectrum. Integrating this expression over wavevectors,

we note that the wave action mean solely depends of group positions distribution

$$\mathbb{E}A(\boldsymbol{x},t) = \iint \mathrm{d}\boldsymbol{x}_r^0 \mathrm{d}\boldsymbol{k}^0 \; N^0(\boldsymbol{x}_r^0,\boldsymbol{k}_r^0) p(\boldsymbol{x}|\boldsymbol{x}_r^0,\boldsymbol{k}^0,t) \tag{4.11}$$

Multi-point action statistics – e.g. focusing $\mathbb{E}\|\nabla_x A\|^2$ – rely on multi-ray correlations, encoded in the stochastic characteristic equations (4.1), but not the simplified model (4.3)-(4.6). Alternatively, Eulerian descriptions of wave action dynamics directly provide action distribution over space and wave vector.

4.2. *Eulerian dynamics and action diffusion*

Wave action spectrum is transported along a 4-dimensional volume-preserving stochastic flow (4.1). Again by analogy with incompressible turbulence (Resseguier *et al.* 2017*a*), the stochastic transport of wave action spectrum in Itō notations reads

$$\begin{aligned} &\partial_t N + (\boldsymbol{v}_g^0 + \overline{\boldsymbol{v}} + \sigma\tfrac{\mathrm{d}B_t}{\mathrm{d}t}) \cdot \boldsymbol{\nabla}_{\boldsymbol{x}} N + \left(-\boldsymbol{\nabla}_{\boldsymbol{x}}(\overline{\boldsymbol{v}} + \sigma\tfrac{\mathrm{d}B_t}{\mathrm{d}t})^{\intercal}\boldsymbol{k}\right) \cdot \boldsymbol{\nabla}_{\boldsymbol{k}} N \\ &= \begin{bmatrix}\boldsymbol{\nabla}_{\boldsymbol{x}} \\ \boldsymbol{\nabla}_{\boldsymbol{k}}\end{bmatrix} \cdot \left(\boldsymbol{D}\begin{bmatrix}\boldsymbol{\nabla}_{\boldsymbol{x}} \\ \boldsymbol{\nabla}_{\boldsymbol{k}}\end{bmatrix} N\right) = \tfrac{1}{2}a_0\Delta_{\boldsymbol{x}} N + \tfrac{1}{2}\gamma_0 \frac{1}{k}\partial_k\left(k^3\partial_k N\right) + \tfrac{3}{2}\gamma_0\partial^2_{\theta_k} N. \end{aligned} \tag{4.12}$$

The RHS is reminiscent to Eq. (3.16) in Bôas & Young (2020) and Eq. (36) in Smit & Janssen (2019), and more generally to rapid wave models. Nevertheless, equation (4.12) is not averaged and explicitly involves large-scale currents and noise terms (terms with factor $\frac{\mathrm{d}B_t}{\mathrm{d}t}$). Differences with Smit & Janssen (2019); Bôas & Young (2020) for the diffusivity estimates and the detailed computation of the 4×4 diffusion matrix $\boldsymbol{D}$ can be found in Appendix. Itō notations of (4.12) explicitly separate mean terms (e.g. diffusion terms) and zero-mean noise terms. Here, the Eulerian Itō notations reveal that coefficients $\frac{1}{2}a_0$, $\frac{1}{2}\gamma_0$, and $\frac{3}{2}\gamma_0$ act to diffuse wave action in space, wavenumber and wave-vector angle, respectively.

5. Numerical experiments

To illustrate these developments, we consider ocean surface gravity waves propagating over a dynamical flow region. Ray tracing through synthetic surface currents will provide a benchmark. It will be shown that a broad range of the current scales can be replaced by the stochastic parametrization (3.10) without affecting ray scattering and action distribution. Theoretical results (4.3)-(4.12) will suggest approximate analytic solutions.

5.1. *Surface current dynamics*

Simplified upper ocean dynamics are considered to follow:

$$(\partial_t + \boldsymbol{v}\cdot\boldsymbol{\nabla})\,\Theta = 0 \;\text{ with }\; \boldsymbol{v} = -\boldsymbol{\nabla}^{\perp}(-\Delta)^{-\xi}\Theta. \tag{5.1}$$

Two extreme cases: the Surface Quasi-Geostrophic dynamics ($\xi = \frac{1}{2}$) (Pierrehumbert 1994; Lapeyre 2017), abbreviated SQG, and the two-dimensional Euler dynamics ($\xi = 1$), abbreviated 2D Euler. SQG is a dynamics with an extreme locality (KE spectrum slope $-5/3$) whereas 2D Euler has an extreme non-locality (KE spectrum slope -3). The objective is to test how the proposed closures apply for both dynamics – and possibly beyond validity of rapid wave models – to also be useful for any more realistic upper ocean dynamics. Additionally, test cases are developed to assess the multiscale stochastic closure in both homogeneous and heterogeneous propagating medium. First, surface fast waves travel in a homogeneous and isotropic SQG turbulence, then waves propagate in a spatially localized 2D Euler turbulence, mimicking an oceanic jet. For both SQG and 2D Euler dynamics, a reference simulation is

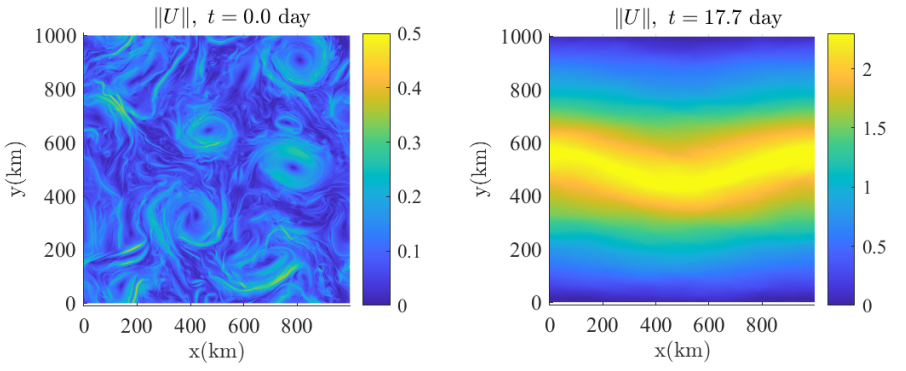

Figure 2: Current velocity norm of the SQG homogeneous turbulence (left) and of the 2D Euler jet current at high-resolution (512×512).

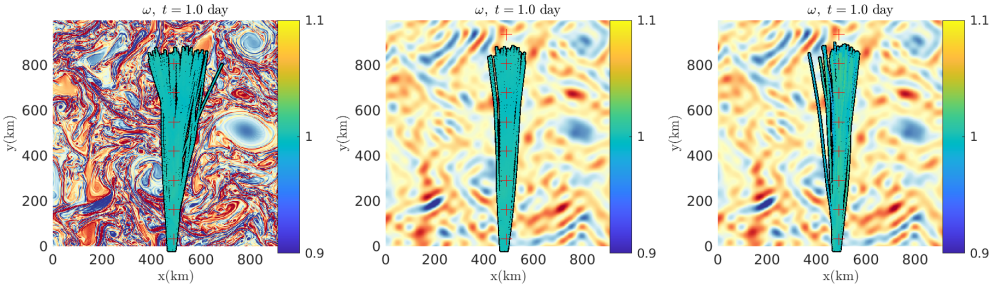

Figure 3: Swell interacting with a high-resolution (512×512) deterministic SQG current (left), a low-resolution (32×32) deterministic SQG current (middle) and a low-resolution (32×32) deterministic SQG current plus (one realization of) the time-uncorrelated stochastic model (right) – colored by the corresponding wave amplitude (right-hand side colorbar) – computed by forward advection and superimposed on the current vorticity $\omega = \boldsymbol{\nabla}^{\perp} \cdot \boldsymbol{v}$. The red cross indicate where the bidirectional wave spectra of figure 4 are computed.

obtained at a resolution 512×512 for a 1000-km squared domain, through a pseudo-spectral code (Resseguier *et al.* 2017*b*, 2020*b*). Once initialized, the current velocity $\boldsymbol{v}$ is about 0.1 m.s^{-1} for the homogeneous turbulence and 1 m.s^{-1} for the jet (see figure 2).

5.2. *Rays scattering in homogeneous SQG turbulence*

A wave system enters the bottom boundary, propagating to the top. The carrier incident wave has an intrinsic wave group velocity of 10 m/s, i.e. wavelength $\lambda = 250$ m. Its envelope is Gaussian with an isotropic spatial extension of 30λ. The left panels of figures 3 and 4 illustrates the resulting branched regime, spreading the wavevectors (figure 4) of the incoming waves. From bottom to top, spectral diffusion occurs (figure 4), in the direction orthogonal (here k_x) to the propagation (here k_y), in line with equation (4.6). This accelerates – along the propagation – the wave position spread (figure 3). This acceleration is explained by the ray equation (4.3) dominated by the intrinsic wave group velocity.

To mimic a badly resolved $\overline{\boldsymbol{v}}$ field, $\boldsymbol{v}$ is smoothed at a resolution 32×32. Using this coarse-scale current, middle panels of figures 3 and 4, the branched regime is strongly depleting, i.e. the spectral small-scale turbulence diffusion is missing. A stochastic current $\boldsymbol{v}'$ is then

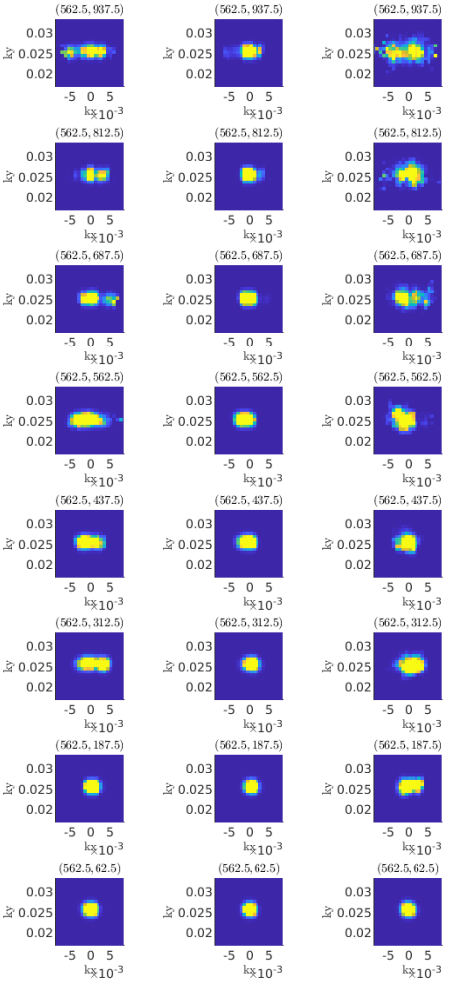

Figure 4: Bidirectional wave spectra, computed by backward advection, at 8 locations along a vertical axis (the mean wave propagation direction) resulting from a swell interacting with a high-resolution (512×512) deterministic SQG current (left), a low-resolution (32×32) deterministic SQG current (middle) and a low-resolution (32×32) deterministic SQG current plus (one realization of) the stochastic model (3.10) (right). The spatial locations where the spectra are calculated are specified on top of each image. We point out these locations on figure 3 by the red crosses.

added for ray tracing (4.1). This stochastic component is divergence-free and has a self-similar distribution of energy across spatial scales (3.10) (see figure 1). The resulting spatial and spectral spreads are now comparable to simulations with high-resolution currents. For this setting, the stochastic closure provides satisfying results for a sufficiently well-resolved large-scale current. The key decorrelation ratio $\epsilon = \frac{l_{\nu'}}{l_\nu} \frac{\|\boldsymbol{v}\|}{v_g^0}$ indeed depends on the resolution through $l_{\nu'}$. The large-scale current $\overline{\boldsymbol{v}}$ is resolved on a 32×32 grid, i.e. with a resolution

$l_{v'} = \frac{\|\boldsymbol{\nabla} \boldsymbol{v}^\mathrm{T}\|}{\|\boldsymbol{\nabla} \boldsymbol{v}'^\mathrm{T}\|} l_v = 0.33\ l_v$. As such $\epsilon = 4.1 \times 10^{-3}$, computed with $v_g^0 \simeq 10$ m.s^{-1} and $\|\boldsymbol{v}\| \simeq 0.12$ m.s^{-1}, so $\frac{\|\boldsymbol{v}\|}{v_g^0} \simeq 1.2 \times 10^{-2}$, which is sufficiently small to make the proposed model applicable.

From the ADSD estimate (equation (3.9) illustrated by figure 1) and (4.7)-(4.8), evaluations of the diffusivity coefficients a_0 and γ_0 are straightforward. Previously discussed Smit & Janssen (2019), the spatial diffusivity is extremely weak: $a_0 = 6.4 \times 10^{-1}$ m^2.s^{-1} (spatial variations in ray equations (4.3)-(4.4) of about $\sqrt{a_0 t} = 230$ m during 1 day). In contrast, the spectral angle diffusivity is large: $3\gamma_0 = 3.0 \times 10^{-8}$ rad^2.s^{-1}. Along our 1-day simulation, neglecting large-scale velocity influence, (4.6) leads to a Brownian wave vector angle variations $\delta\theta_k = \theta_k - \theta_k(0) = \sqrt{3\gamma_0} B_t^{(4)}$ with a standard deviation $\sigma_{\delta\theta_k} = \sqrt{3\gamma_0 t} = 5.2 \times 10^{-2}$ rad $\approx 3.0°$, eventually increasing the wave group spectral maximal extension from $\pm 2\sigma_{k_x} = \pm 2 \frac{2\pi}{30\lambda} = \pm 1.7 \times 10^{-3}$ rad.m^{-1} to $\pm 2\sigma_{k_x} \approx \pm 2\sqrt{\left(\frac{2\pi}{30\lambda}\right)^2 + \left(k\sigma_{\delta\theta_k}\right)^2} = \pm 3.1 \times 10^{-3}$ rad.m^{-1}, confirmed by figure 4. This figure also illustrates the wave action diffusion induced by diffusivity γ_0, well predicted by the Eulerian wave action model (4.12). In the branched regime, the increased angle variability leads, by advection, to a spatial spread. The simplified ray equation (4.3) gives $\delta x \approx \int_0^t v_g^0 \cos\theta_k \approx v_g^0 \int_0^t \delta\theta_k \approx v_g^0 \sqrt{3\gamma_0} \int_0^t B_{t'}^{(4)}$ with maximal extension $\pm 2\sigma_x \approx \pm 2 v_g^0 \sqrt{\gamma_0 t^3} \approx \pm 52$ km, in agreement with figure 3. Finally, we estimate a first-order delay along the propagation $\delta t = t - (y - y(0))/v_g^0 \approx \int_0^t (1 - \sin\theta_k) \approx \frac{1}{2}\int_0^t \delta\theta_k^2 \approx \frac{3}{2}\gamma_0 \int_0^t (B_{t'}^{(4)})^2$, with mean value $\mathbb{E}\delta t = \frac{3}{4}\gamma_0 t^2$.

5.3. *Wave groups trapped in a 2D Euler turbulent jet*

Tests are now performed for rays traveling in fast and strongly heterogeneous 2D Euler flows. Classical fast wave models – assuming flows of weak amplitude and often uniform statistics – are expected to fail here. Jets exhibit strong current gradients (e.g. Kudryavtsev *et al.* 2017) creating strong ray focusing and possibly rogue events. Passing through localized spatial structures, caustics can appear but solely from unrealistically collimated wave trains (White & Fornberg 1998; Heller *et al.* 2008; Wang *et al.* 2023). Occurrences strongly reduce for finite directional spread (Slunyaev & Shrira 2023). Here, wave groups are trapped in a jet, but nonlinear wave interactions are neglected. The high-resolution numerical simulations (see figure 5) reveal that even linear wave trains are well trapped in adversarial currents. Freund & Fleischman (2002) observed a similar behavior for acoustic waves in a 3D turbulent jet. Note that during our simulation, rays cross the domain several times (because of the doubly periodic boundary conditions, see appendix for technical details). Top (resp. bottom) of the jet, the vorticity and thus – at first order – rays curvatures (Dysthe 2001) are negative (resp. positve). Therefore, rays oscillate around the jet. A toy model can explain this behavior. Following the multiscale stochastic approach (4.3)-(4.6), wave scattering is also taken into account.

For very-coarsed-grained (4×4) current $\overline{\boldsymbol{v}}$, oscillation remains, but most of the scattering vanishes, as illustrated by figure 6. Moreover, the curvature of the jet creates artificial wave focusing at $t = 8$ and 10 days. Introducing a time-uncorrelated model (3.10) corrects the resolution issue on figure 7. Figure 8 plots the current ADSD. The current is strong ($\|\boldsymbol{v}\| \simeq 1.4$ m.s^{-1}), and the usual fast wave approximation cannot be applied ($\frac{\|\boldsymbol{v}\|}{v_g^0} \simeq 1.2 \times 10^{-1}$). However, the proposed modified fast wave model is valid, even at the very coarse 4×4 resolution. Indeed, 2D Euler spectra are steeper than for SQG dynamics, and the length scale ratio is

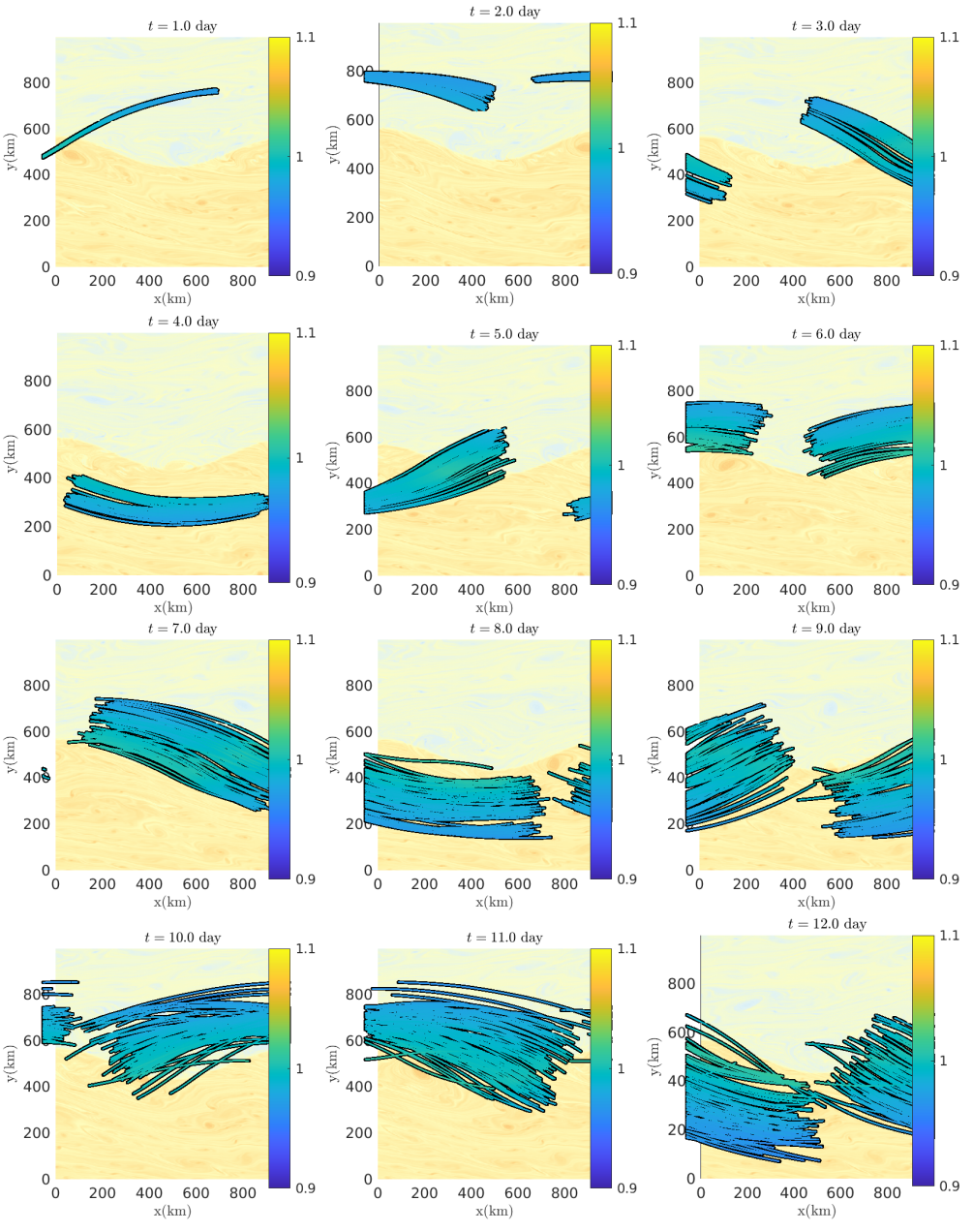

Figure 5: Rays facing a high-resolution (512×512) deterministic 2D Euler jet current – colored by the corresponding wave amplitude (right-hand side colorbar) – computed by forward advection and superimposed on the current vorticity $\omega = \boldsymbol{\nabla}^{\perp} \cdot \boldsymbol{\nu}$.

already significant at this resolution, $\frac{l_{\nu'}}{l_\nu} = 0.14$, and the derived time-decorrelation ratio is small: $\epsilon = \frac{l_{\nu'}}{l_\nu} \frac{\|\boldsymbol{\nu}\|}{v_g^0} = 1.6 \times 10^{-2}$.

Furthermore, by approximating the under-resolved current $\overline{\nu}$, an analytic stochastic solution can be obtained for a ray traveling against the current. The large-scale pattern of the jet takes

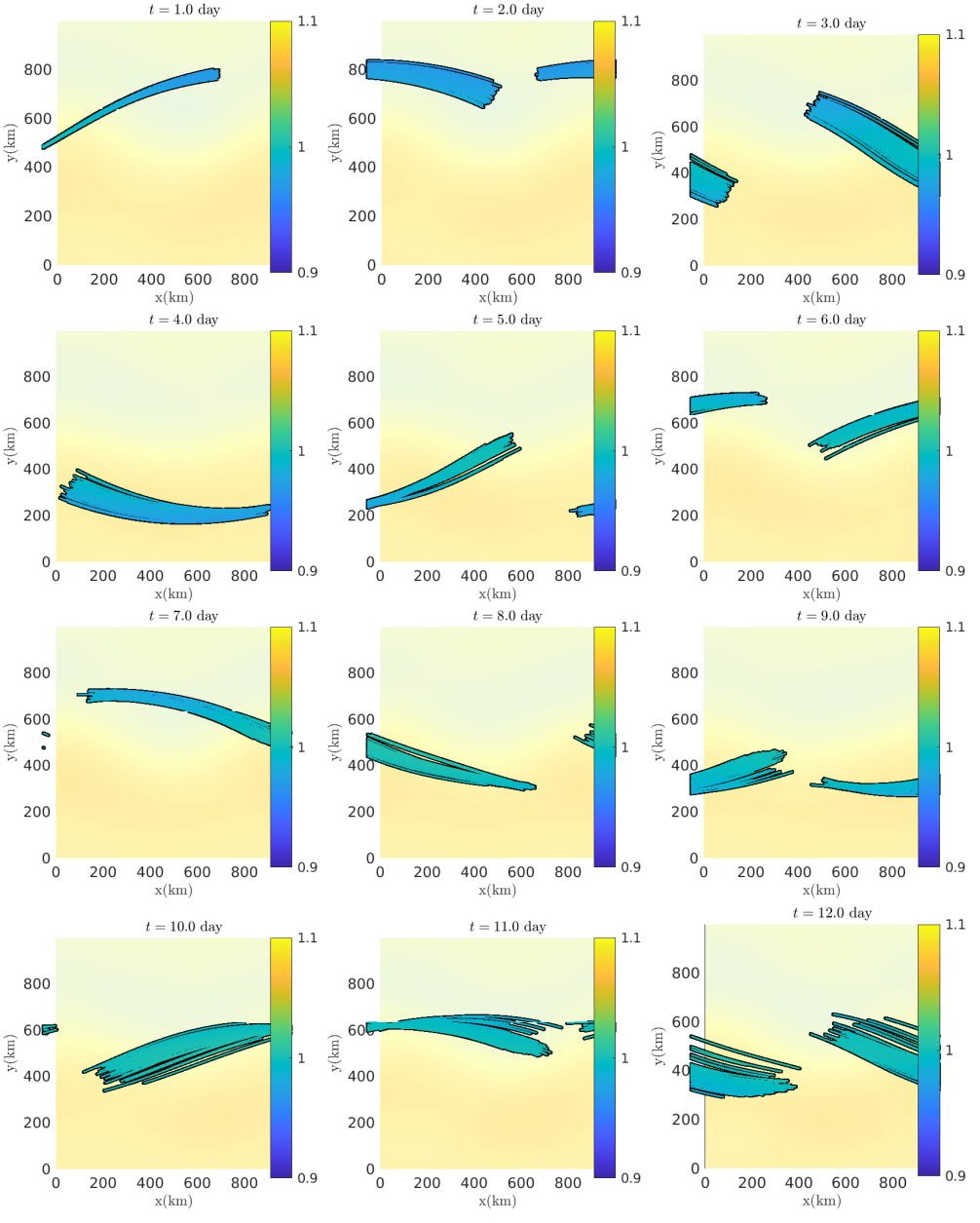

Figure 6: Rays facing a low-resolution (4×4) deterministic 2D Euler jet current – colored by the corresponding wave amplitude (right-hand side colorbar) – computed by forward advection and superimposed on the current vorticity $\omega = \boldsymbol{\nabla}^{\perp} \cdot \boldsymbol{v}$.

a quadratic form

$$\overline{u} \approx \overline{U}_0 - \tfrac{1}{2}\overline{\beta}\left(y - \frac{L_y}{2}\right)^2 \quad \text{and} \quad \overline{v} \approx 0, \quad \text{with} \quad \overline{U}_0, \overline{\beta} < 0 \tag{5.2}$$

Note, the toy model (5.2) simply considers a straight jet, neglecting its curvature. For weak subgrid currents and a ray, $(x_r, y_r' + \frac{L_y}{2}, k, \theta_k)$, propagating mainly to the right, θ_k is small

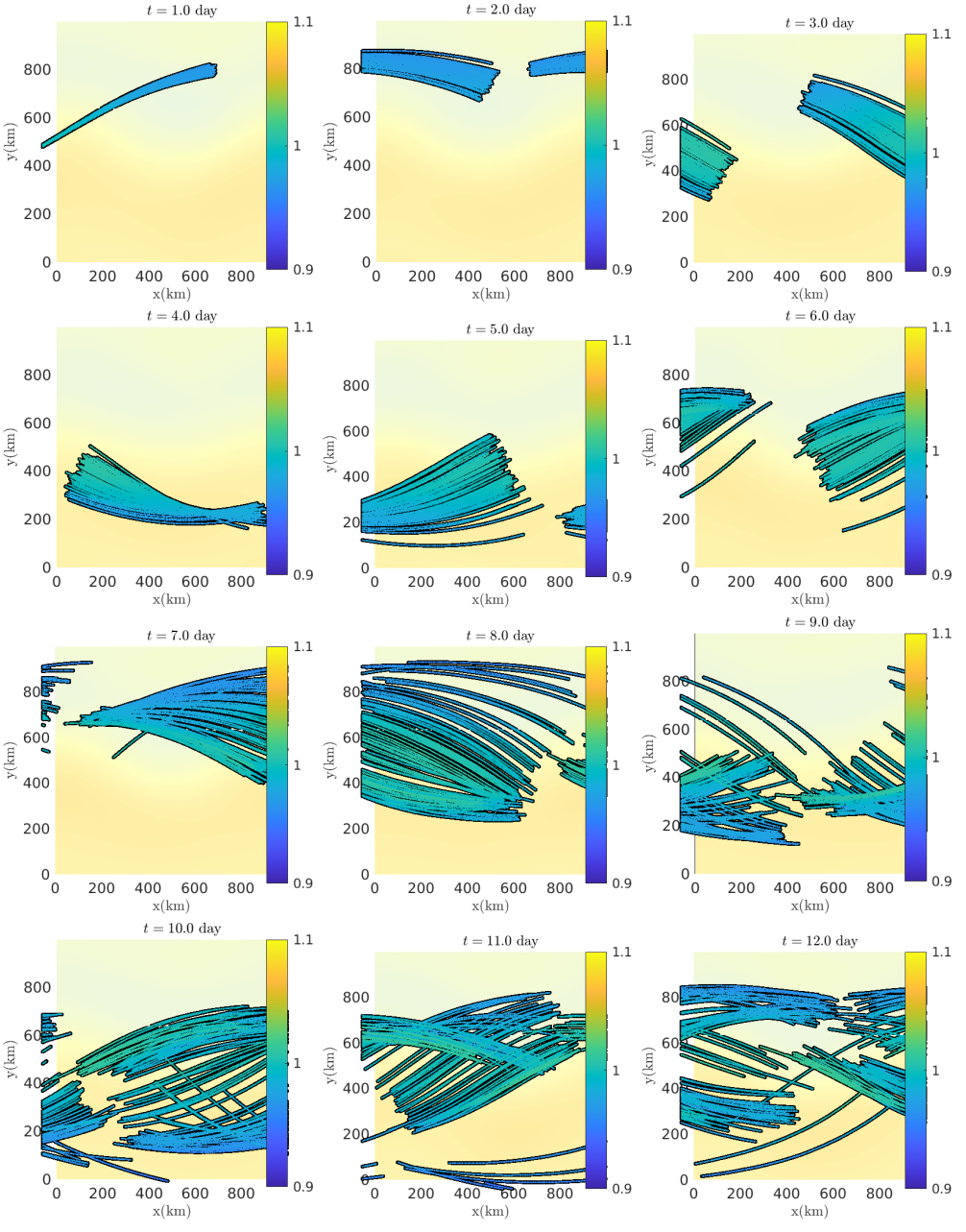

Figure 7: Rays facing a low-resolution (4×4) deterministic 2D Euler jet current plus (one realization of) the time-uncorrelated stochastic model – colored by the corresponding wave amplitude (right-hand side colorbar) – computed by forward advection and superimposed on the current vorticity $\omega = \boldsymbol{\nabla}^{\perp} \cdot \boldsymbol{v}$.

and the simplified ray equation (4.4) determines the group position with respect to the jet y_r'

$$\frac{\mathrm{d}}{\mathrm{d}t} y_r' \approx v_g^0 \sin(\theta_k) = v_g^0 \theta_k + O(\theta_k^2). \tag{5.3}$$

For frozen turbulence, the wave-number and hence v_g^0 will not significantly vary. The other

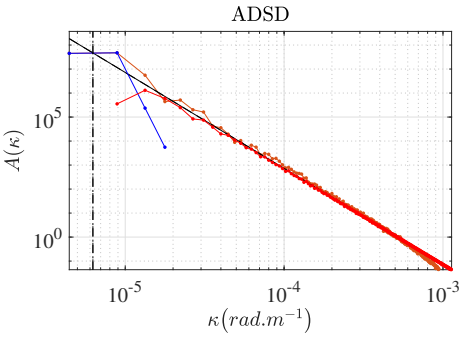

Figure 8: ADSD ($m^2.s^{-1}/(\mathrm{rad}.m^{-1})$) of the resolved high-resolution jet velocity in brown, low-resolution jet velocity in blue, and modeled stochastic velocity, in red. The theoretical spectrum slope −3 (black solid line) is imposed, consistent with homogeneous 2D Euler dynamics. The residual ADSD (red line) is set to extrapolate that power law at small scales.

ray equation (4.3) localizes the group along the jet, $x_r \approx x_r(0) + (v_g^0 - \overline{u})t$, dropping the $O(\theta_k^2)$ from now on. Moreover, $\tilde{\boldsymbol{k}}^\perp \cdot \boldsymbol{\nabla}\overline{\boldsymbol{v}}^\mathsf{T}\tilde{\boldsymbol{k}} \approx -\partial_y\overline{u}$ and the dynamics of wave vector angle (4.6) simplifies to a stochastic oscillator equation:

$$\frac{\mathrm{d}^2}{\mathrm{d}t^2}y_r' = v_g^0\frac{\mathrm{d}}{\mathrm{d}t}\theta_k = -\partial_y(v_g^0\overline{u}) + v_g^0\sqrt{3\gamma_0}\dot{B}_t^{(4)} = -\overline{\omega}_r^2 y_r' + v_g^0\sqrt{3\gamma_0}\dot{B}_t^{(4)}. \tag{5.4}$$

with $\overline{\omega}_r = \sqrt{|v_g^0\overline{\beta}|}$. Here $v_g^0\overline{u}$ plays the role of a potential, trapping the rays in the jet vicinity, whereas the noise accounts for wave scattering. Solution of this linear equation is known (e.g. Resseguier *et al.* 2017*a*, Eq.(51)-(55)):

$$y_r(t) = \underbrace{\frac{L_y}{2} + y_r'(0)\cos(\overline{\omega}_r t) + \frac{v_g^0}{\overline{\omega}_r}\theta_k(0)\sin(\overline{\omega}_r t)}_{=\mathbb{E}(y_r(t))} + \underbrace{Y_{\gamma_0}\sqrt{\overline{\omega}_r}\int_0^\tau \sin\big(\overline{\omega}_r(t-r)\big)\mathrm{d}B_r^{(4)}}_{=y_r''(t)}, \tag{5.5}$$

with $Y_{\gamma_0} = v_g^0\sqrt{3\gamma_0/\overline{\omega}_r^3}$. The wavevector angle solution is similar. The solution ensemble mean, $\mathbb{E}y_r$, is a simple coherent deterministic oscillator. This mean solution describes well the interaction between the group and the under-resolved current from figure 6. From the coarse-scale vorticity shear plotted in figure 9 in the vicinity of the jet, we can estimate $\overline{\beta} = -2.7\times10^{-11}\mathrm{m}^{-1}.\mathrm{s}^{-1}$. It yields an oscillation frequency $\overline{\omega}_r = 1.3\times10^{-5}\mathrm{rad}.\mathrm{s}^{-1}$ i.e. a period of $2\pi/\overline{\omega}_r = 5.7$ days, in agreement with the ray tracing simulations. Note that the high-resolution vorticity shear, left panel of figure 9, does not suggest any relevant values to explain the ray oscillations. Only the proposed multiscale current decomposition provides a quantitative explanation for these oscillations, and by extension for trapping rays inside the jet. Added to the mean solution, the random parts, $y_r''(t)$, are continuous summations of zero-mean incoherent wave fluctuations. At each time r, the additive random forcing introduces an oscillation. But, the influence of the past excitations is weighed by sine wave due to the phase change. The group position and wavevector angle are Gaussian random variables (as linear combinations of independent Gaussian variables). Therefore, their finite dimensional law (*i.e.* the multi-time probability density function) are entirely defined by their mean and covariance functions. Specifically,

$$\mathbb{E}\left(y_r''(t)y_r''(t+\tau)\right) = \tfrac{1}{4}Y_{\gamma_0}^2\big(\cos(\overline{\omega}_r\tau)\,(2\overline{\omega}_r t - \sin(2\overline{\omega}_r t)) + \sin(\overline{\omega}_r\tau)\,(1-\cos(2\overline{\omega}_r t))\big). \tag{5.6}$$

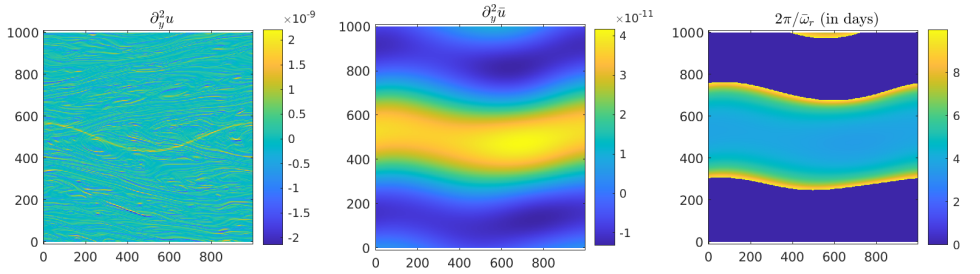

Figure 9: Vorticity shear $\partial_y^2 u$ of the deterministic 2D Euler jet current at high-resolution (512×512) (left), at low-resolution (4×4) (middle), and the corresponding swell system period $2\pi/\overline{\omega}_r$. Far from the jet (±200 km away), the vorticity shear becomes zero or even positive, so period larger than 10 days are cropped.

In particular, the variance of the vertical positions reads $\sigma_y^2(t) = \frac{1}{4} Y_{\gamma_0}^2 \, (2\overline{\omega}_r t - \sin(2\overline{\omega}_r t))$. At $t = 2\pi/\overline{\omega}_r$, the group has oscillated once around the jet and the maximal position extension reaches $\pm 2\sigma_y = \pm 2\sqrt{\pi}\ Y_{\gamma_0} = \pm 42$ km, well confirmed by ray simulations. In contrast, usual fast wave models (e.g. Smit & Janssen 2019) do not consider the interplay between smooth and rough currents, and hence solely predict a classical branched regime with a much faster vertical location spreading: $\pm 2\sigma_y = \pm 2\sqrt{(2\pi)^3/3}\ Y_{\gamma_0} = \pm 217$ km. For large time, our multiscale approach predicts a scaling in t, much slower than the usual t^3 scaling of the branched regime.

From the group vertical location and wavevector angle, we can also solve (4.5) analytically to estimate the group wavenumber variations. For small wavevector angles, $-\int_0^t \overline{\sigma} \sin(\zeta) \approx 2 \int_0^t \overline{\omega} \theta_k = 2\overline{\beta} \int_0^t y_r' \theta_k$ and (4.9) together with the analytic solutions for y_r' and θ_k give a closed stochastic expression for the group wavenumber. Thus, the wavenumber factor $\exp(2\overline{\beta} \int_0^t y_r' \theta_k)$ oscillates at frequency $2\overline{\omega}_r$ and the oscillations modulate the wave amplitude: $h = \sqrt{E} = \sqrt{\omega_0 N} = \text{cst.} k^{\frac{1}{4}}$. The modulations are associated with wave-current energy exchanges Boury *et al.* (2023), visible in the colored rays, figures 5, 6 and 7, when the groups enter and exit the jet.

Finally, the conditional ray distribution, $p(\boldsymbol{x}, \boldsymbol{k} | \boldsymbol{x}_r^0, \boldsymbol{k}^0, t)$, the action spectrum mean from (4.10) and the action mean from (4.11) can all be derived. For a system initially localized in $(0, \frac{L_y}{2})$ with action A^0, wavenumber k^0 and a $\sigma_{\delta\theta_k}^0$-width Gaussian angular spreading, propagating to the right, the action mean reads

$$\mathbb{E}A(x, y, t) = A^0 \delta \left(x - (v_g^0(k^0) - \overline{u}(y))t \right) \mathcal{N} \left(y - \tfrac{L_y}{2} | \tilde{\sigma}_y^2(t) \right), \tag{5.7}$$

with $\mathcal{N}\left(\bullet | \tilde{\sigma}_y^2(t) \right)$, a Gaussian function with variance $\tilde{\sigma}_y^2(t) = \sigma_y^2(t) + \left(\frac{v_g^0}{\overline{\omega}_r} \sin(\overline{\omega}_r t) \sigma_{\delta\theta_k}^0 \right)^2$. The action is advected in the horizontal direction, and slowly diffuses along the vertical direction.

6. Conclusion

Developed to generalize the ray-path concept for waves propagating over an heterogeneous turbulence, a practical stochastic framework is derived. For fast waves, the smallest scales of a turbulent flow decorrelate along the wave propagation. Flows with steeper spectra

decorrelate faster, leading to a broader validity range of fast wave approximations. The proposed framework encodes both large-scale refraction and random scattering effects on wave statistical properties. The mean wave-action statistics are directly linked to resolved strain-rate and vorticity, but also to unresolved KE spectral properties. Both Eulerian and Lagrangian views are presented. A convenient calibration method is also proposed for the subgrid parametrization.

Anticipated, random horizontal currents delay wave arrival and augment the initial radiative transport equation with a directional diffusive term. These phenomena are illustrated with numerical simulations, analytical solutions, and quantitative proxies describing weak homogeneous turbulence. Using these proxies, measured delays in ray arrivals, estimated wave energy spectral characteristics and decays, and/or varying directional spread shall then be used to more quantitatively interpreted the upper the turbulent underlying flow properties.

The generalized fast wave approximation does takes into account wavenumber variation and handles strong heterogeneous flows, like localized jets with strong current gradients. As compared to numerical simulations, numerical and theoretical results explain and quantify ray trapping effects by jets, unlike usual fast wave approaches.

Among fast wave literature, isotropic diffusion and, hence, wavenumber diffusion may (e.g. Voronovich 1991) or may not (e.g. Bôas & Young 2020) comes into play (see last Appendix for details). Future works could adapt our convenient stochastic calculus framework to the second models family. Besides, further analytical developments could consider finite-size wave groups, their dynamics (Jonsson 1990; White & Fornberg 1998) and statistical distributions, or alternatively the Eulerian action dynamics (4.12) with all its multi-point stochastic structure. When achieved, this next theoretical development could provide new means to analyze wave dynamics with subsequent fast simulations of ensembles. Beside comprehension and analysis, our stochastic simulation tools aim at eventually facilitate future ensemble-based data assimilation algorithms (Smit *et al.* 2021).

Funding. This work is supported by the R&T CNES R-S19/OT-0003-084, the ERC project 856408-STUOD, the European Space Agency World Ocean Current project (ESA Contract No. 4000130730/20/I-NB), and SCALIAN DS.

Declaration of interests. The authors report no conflict of interest.

Data availability statement. SCALIAN DS owns a portion of the developed code intellectual property. For commercial reasons, that code will remains private.

Author ORCIDs. V. Resseguier, https://orcid.org/0000-0002-9301-9493; E. Hascoët https://orcid.org/0009-0002-0760-6534; B. Chapron, https://orcid.org/0000-0001-6088-8775

Author contributions. VR developed the theory. VR and EH wrote the code and performed numerical experiments. VR and BC wrote the paper.

Appendix A. Stochastic forcing covariance

In this appendix, we will compute the conditionnal covariance of the stochastic forcing of our eikonal characteristic equations (4.1), that is:

$$2\boldsymbol{D} \triangleq \tfrac{1}{\mathrm{d}t}\mathbb{E}_t\left\{\begin{pmatrix}\sigma\mathrm{d}B_t\\ \mathrm{d}\boldsymbol{\eta}_t\end{pmatrix}\begin{pmatrix}\sigma\mathrm{d}B_t\\ \mathrm{d}\boldsymbol{\eta}_t\end{pmatrix}^{\mathsf{T}}\right\} = \begin{bmatrix}\boldsymbol{a} & \Sigma_{\eta,\sigma}\\ \Sigma_{\eta,\sigma}^{\mathsf{T}} & \Sigma_\eta\end{bmatrix} \tag{A 1}$$

where, $d\boldsymbol{\eta}_t = -\boldsymbol{\nabla}(\sigma\mathrm{d}B_t)^{\mathsf{T}}\boldsymbol{k}$, denotes the wave-vector stochastic forcing and, $\Sigma_\eta\mathrm{d}t$, its covariance, and $\mathbb{E}_t\{\bullet\} \triangleq \mathbb{E}\{\bullet|\boldsymbol{x}_r(t),\boldsymbol{k}(t)\}$ stands for the conditional expectation evaluated with given characteristics $(\boldsymbol{x}_r(t),\boldsymbol{k}(t))$ at the current time t. Note that in the appendix we use Itō notations only.

The subgrid velocity, $\boldsymbol{v}' = \sigma \mathrm{d}B_t/\mathrm{d}t$ is constructed in Fourier space with a divergence-free isotropic spatial filter $\boldsymbol{\nabla}^\perp \psi_\sigma$ (see (3.10)).

$$\widehat{\boldsymbol{v}'}(\boldsymbol{\kappa}, t) = \int \mathrm{d}\boldsymbol{x}\ \boldsymbol{v}'(\boldsymbol{x}, t) e^{-\mathrm{i}\boldsymbol{\kappa}\cdot\boldsymbol{x}} = \widehat{\sigma \mathrm{d}B_t}/\mathrm{d}t(\boldsymbol{\kappa}, t) = \mathrm{i}\boldsymbol{\kappa}^\perp \widehat{\tilde{\psi}}_\sigma(\kappa)\widehat{\mathrm{d}B_t}(\boldsymbol{\kappa})/\mathrm{d}t, \tag{A 2}$$

The computation of the variance tensor $\boldsymbol{a}$ is classical and straightforward from the definition of the inverse Fourier transform and the identity $\mathbb{E}\left\{\widehat{\mathrm{d}B_t}(\boldsymbol{\kappa}_1)\overline{\widehat{\mathrm{d}B_t}}(\boldsymbol{\kappa}_2)\right\} = (2\pi)^2\delta(\boldsymbol{\kappa}_1 - \boldsymbol{\kappa}_2)\mathrm{d}t$. We simply need to split the integral of the stochastic forcing spectrum over the current wavevector $\boldsymbol{\kappa} = \kappa(\cos\theta_\kappa, \sin\theta_\kappa)$:

$$\boldsymbol{a} = \frac{1}{(2\pi)^4 \mathrm{d}t} \iint \mathrm{d}\boldsymbol{\kappa}_1 \mathrm{d}\boldsymbol{\kappa}_1\ \mathbb{E}_t\left\{\widehat{\sigma \mathrm{d}B_t}(\boldsymbol{\kappa}_1, \boldsymbol{k})\overline{\widehat{\sigma \mathrm{d}B_t}^\mathsf{T}(\boldsymbol{\kappa}_2, \boldsymbol{k})}\right\} e^{\mathrm{i}(\boldsymbol{\kappa}_1 - \boldsymbol{\kappa}_2)\cdot\boldsymbol{x}}, \tag{A 3}$$

$$= \frac{1}{(2\pi)^2} \int \mathrm{d}\boldsymbol{\kappa}\ \kappa^2 |\widehat{\tilde{\psi}}_\sigma(\kappa)|^2 \begin{pmatrix} -\sin\theta_\kappa \\ \cos\theta_\kappa \end{pmatrix} \begin{pmatrix} -\sin\theta_\kappa \\ \cos\theta_\kappa \end{pmatrix}^\mathsf{T}, \tag{A 4}$$

$$= \frac{1}{(2\pi)^2} \int_0^\infty \oint_0^{2\pi} \mathrm{d}\kappa \mathrm{d}\theta_\kappa \kappa^3 |\widehat{\tilde{\psi}}_\sigma(\kappa)|^2 \begin{pmatrix} \sin^2\theta_\kappa & -\sin\theta_\kappa\cos\theta_\kappa \\ -\sin\theta_\kappa\cos\theta_\kappa & \cos^2\theta_\kappa \end{pmatrix}, \tag{A 5}$$

$$= \frac{2}{2\pi} a_0 \oint_0^{2\pi} \mathrm{d}\theta_\kappa \begin{pmatrix} \sin^2\theta_\kappa & -\sin\theta_\kappa\cos\theta_\kappa \\ -\sin\theta_\kappa\cos\theta_\kappa & \cos^2\theta_\kappa \end{pmatrix}, \tag{A 6}$$

$$= a_0 \mathbb{I}_d. \tag{A 7}$$

Now, the Fourier transform of the wave-vector stochastic forcing is

$$\mathrm{d}\widehat{\boldsymbol{\eta}}_t = -\widehat{\boldsymbol{\nabla}(\sigma \mathrm{d}B_t)^\mathsf{T}}\boldsymbol{k} = -\mathrm{i}\boldsymbol{\kappa}(\mathrm{i}\boldsymbol{\kappa}^\perp \widehat{\tilde{\psi}}_\sigma \widehat{\mathrm{d}B_t}) \cdot \boldsymbol{k} = -\boldsymbol{\kappa}(\boldsymbol{k}^\perp \cdot \boldsymbol{\kappa})\widehat{\tilde{\psi}}_\sigma \widehat{\mathrm{d}B_t}. \tag{A 8}$$

Then, applying the crest-oriented rotation matrix, $\boldsymbol{M}_k = \begin{bmatrix} \tilde{\boldsymbol{k}} & \tilde{\boldsymbol{k}}^\perp \end{bmatrix}$, leads to

$$\mathrm{d}\widehat{\boldsymbol{Z}}_t = \boldsymbol{M}_k^\mathsf{T} \mathrm{d}\widehat{\boldsymbol{\eta}}_t = -\begin{pmatrix} \tilde{\boldsymbol{k}} \cdot \boldsymbol{\kappa} \\ \tilde{\boldsymbol{k}}^\perp \cdot \boldsymbol{\kappa} \end{pmatrix} (\boldsymbol{k}^\perp \cdot \boldsymbol{\kappa}) \widehat{\tilde{\psi}}_\sigma \widehat{\mathrm{d}B_t} = -\begin{pmatrix} \cos\delta\theta \sin\delta\theta \\ \sin^2\delta\theta \end{pmatrix} \kappa^2 k\ \widehat{\tilde{\psi}}_\sigma \widehat{\mathrm{d}B_t}, \tag{A 9}$$

with $\delta\theta = \theta_\kappa - \theta_k$. From there, we can evaluate the conditional covariance matrix $\Sigma_Z = \frac{1}{\mathrm{d}t}\mathbb{E}_t\left\{\mathrm{d}\boldsymbol{Z}_t \mathrm{d}\boldsymbol{Z}_t^\mathsf{T}\right\}$ of $\mathrm{d}\boldsymbol{Z}_t$ as before:

$$\Sigma_Z = \frac{1}{(2\pi)^4 \mathrm{d}t} \iint \mathrm{d}\boldsymbol{\kappa}_1 \mathrm{d}\boldsymbol{\kappa}_1\ \mathbb{E}_t\left\{\mathrm{d}\widehat{\boldsymbol{Z}}_t(\boldsymbol{\kappa}_1, \boldsymbol{k})\overline{\mathrm{d}\widehat{\boldsymbol{Z}}_t^\mathsf{T}(\boldsymbol{\kappa}_2, \boldsymbol{k})}\right\} e^{\mathrm{i}(\boldsymbol{\kappa}_1 - \boldsymbol{\kappa}_2)\cdot\boldsymbol{x}}, \tag{A 10}$$

$$= \frac{1}{(2\pi)^2} \int_0^\infty \oint_0^{2\pi} \mathrm{d}\kappa \mathrm{d}\delta\theta\ \kappa^5 k^2 |\widehat{\tilde{\psi}}_\sigma(\kappa)|^2 \begin{pmatrix} \cos^2\delta\theta \sin^2\delta\theta & \cos\delta\theta \sin^3\delta\theta \\ \cos\delta\theta \sin^3\delta\theta & \sin^4\delta\theta \end{pmatrix}, \tag{A 11}$$

$$= \gamma_0 k^2 \begin{bmatrix} 1 & 0 \\ 0 & 3 \end{bmatrix}. \tag{A 12}$$

Finally, we come back to the canonical frame to get Σ_η

$$\Sigma_\eta = \mathbb{E}_t\left\{\mathrm{d}\boldsymbol{\eta}_t \mathrm{d}\boldsymbol{\eta}_t^\mathsf{T}\right\} = \boldsymbol{M}_k \Sigma_Z \boldsymbol{M}_k^\mathsf{T} = \gamma_0 k^2 \left[\tilde{\boldsymbol{k}}\tilde{\boldsymbol{k}}^\mathsf{T} + 3\tilde{\boldsymbol{k}}^\perp \left(\tilde{\boldsymbol{k}}^\perp\right)^\mathsf{T}\right] \tag{A 13}$$

For noises cross-correlations, by isotropy, it is also straightforward to show that

$$\Sigma_{\eta,\sigma} = 0. \tag{A 14}$$

The stochastic forcings of $\boldsymbol{x}_r$ and $\boldsymbol{k}$ are hence (conditionally) independent from one another.

Appendix B. Single ray dynamics

The Itō noise $\begin{pmatrix}\sigma \mathrm{d}B_t \\ \mathrm{d}\boldsymbol{\eta}_t\end{pmatrix}$ is white in time and conditionally Gaussian. Its conditional single-point distribution is fully determined by its zero mean and its local covariance matrix (given by equations (A 1), (A 7), (A 13) and (A 14)). In particular, we can replace this noise by another zero-mean Gaussian vector with the same covariance without changing the single-ray dynamics – typically replacing $\sigma \mathrm{d}B_t$ by $\sqrt{a_0}\begin{pmatrix}\mathrm{d}B_t^{(1)} \\ \mathrm{d}B_t^{(2)}\end{pmatrix}$ and $\mathrm{d}\boldsymbol{Z}_t$ by $-\sqrt{\gamma_0}k\begin{pmatrix}\mathrm{d}B_t^{(3)} \\ \sqrt{3}\mathrm{d}B_t^{(4)}\end{pmatrix}$. It yields the simplified ray equations (4.3)-(4.4).

Then note that from Itō lemma (Oksendal 1998) $\mathrm{d}\tilde{\boldsymbol{k}} = \mathrm{d}\begin{pmatrix}\cos\theta_k \\ \sin\theta_k\end{pmatrix} = \tilde{\boldsymbol{k}}^{\perp}\mathrm{d}\theta_k - \frac{1}{2}\tilde{\boldsymbol{k}}\mathrm{d} < \theta_k, \theta_k >_t$ where $< \bullet, \bullet >_t$ denotes the quadratic covariation. Thus,

$$\mathrm{d}\boldsymbol{k} = \mathrm{d}k\tilde{\boldsymbol{k}} + k\mathrm{d}\tilde{\boldsymbol{k}} + \mathrm{d} < k, \tilde{\boldsymbol{k}} >= (\mathrm{d}k - \tfrac{1}{2}k\mathrm{d} < \theta_k, \theta_k >_t)\tilde{\boldsymbol{k}} + (k\mathrm{d}\theta_k + \mathrm{d} < k, \theta_k >_t)\tilde{\boldsymbol{k}}^{\perp} \quad \text{(B 1)}$$

Projecting this equation and $\mathrm{d}\boldsymbol{k} = -\boldsymbol{\nabla}\overline{\boldsymbol{v}}^{\mathsf{T}}\boldsymbol{k}\mathrm{d}t + \mathrm{d}\boldsymbol{\eta}_t$ on $\tilde{\boldsymbol{k}}$ and $\tilde{\boldsymbol{k}}^{\perp}$, we have

$$\begin{cases}\mathrm{d}k = -\tilde{\boldsymbol{k}}\cdot\boldsymbol{\nabla}\overline{\boldsymbol{v}}^{\mathsf{T}}\boldsymbol{k}\mathrm{d}t + (\mathrm{d}Z_t)_1 + \frac{1}{2}k\mathrm{d} < \theta_k, \theta_k >_t \\ k\mathrm{d}\theta_k = -\tilde{\boldsymbol{k}}^{\perp}\cdot\boldsymbol{\nabla}\overline{\boldsymbol{v}}^{\mathsf{T}}\boldsymbol{k}\mathrm{d}t + (\mathrm{d}Z_t)_2 - \mathrm{d} < k, \theta_k >_t\end{cases}, \quad \text{(B 2)}$$

$$\begin{cases}\mathrm{d}k = -\tilde{\boldsymbol{k}}\cdot\boldsymbol{\nabla}\overline{\boldsymbol{v}}^{\mathsf{T}}\boldsymbol{k}\mathrm{d}t + (\mathrm{d}Z_t)_1 + \frac{1}{2}k^{-1}\mathrm{d} < Z_2, Z_2 >_t \\ \mathrm{d}\theta_k = -\tilde{\boldsymbol{k}}^{\perp}\cdot\boldsymbol{\nabla}\overline{\boldsymbol{v}}^{\mathsf{T}}\tilde{\boldsymbol{k}}\mathrm{d}t + k^{-1}(\mathrm{d}Z_t)_2 + \frac{1}{2}k^{-2}\mathrm{d} < Z_1, Z_2 >_t\end{cases}. \quad \text{(B 3)}$$

The treatment of the large-scale terms $\tilde{\boldsymbol{k}}\cdot\boldsymbol{\nabla}\overline{\boldsymbol{v}}^{\mathsf{T}}\tilde{\boldsymbol{k}}$ and $\tilde{\boldsymbol{k}}^{\perp}\cdot\boldsymbol{\nabla}\overline{\boldsymbol{v}}^{\mathsf{T}}\tilde{\boldsymbol{k}}$ is classical. Interested readers can refer to Lapeyre *et al.* (1999) for details. From Ito lemma again, $\mathrm{d}\log k = \mathrm{d}k/k - \frac{1}{2}\mathrm{d} < k, k >_t/k^2$ leading to the simplified wave-vector dynamics (4.5)-(4.6).

Appendix C. Subgrid flow anisotropy and comparison with other works

Throughout this paper, we have considered an isotropic model for the stochastic subgrid velocity (3.10). The isotropic diffusivity matrix $\boldsymbol{a} = a_0\mathbb{I}_d$ is a good illustration of this. In contrast, many authors (e.g. White & Fornberg 1998; Bôas & Young 2020; Smit & Janssen 2019) assume isotropic and homogeneous turbulence and obtain anisotropic stochastic subgrid models for $\frac{\|\boldsymbol{v}\|}{v_g^0} \to 0$. In these approaches, the integral over $\delta\theta$ in diffusivity matrix computations (A 4) and (A 12) involve singular integrations over the direction $\boldsymbol{v}_g^0 = v_g^0\tilde{\boldsymbol{k}}$. It makes appear a Dirac delta function, $2\pi\delta(\boldsymbol{\kappa}\cdot\boldsymbol{v}_g^0) = \frac{2\pi}{\kappa v_g^0}(\delta(\theta_\kappa - \theta_k - \frac{\pi}{2}) + \delta(\theta_\kappa - \theta_k + \frac{\pi}{2}))$ (see Appendix in Bôas & Young 2020). This precision imposes a statistical anisotropy for $\boldsymbol{\sigma}\mathrm{d}B_t$ (oriented along $\boldsymbol{k}$) and $d\boldsymbol{\eta}_t$ (oriented along $\boldsymbol{k}^{\perp}$), eventually leading to a covariance $\Sigma_Z = \gamma_0 k^2\begin{bmatrix}0 & 0 \\ 0 & 16\end{bmatrix}$ (Eq. (3.17) in Bôas & Young (2020) and Eq. (24) in Smit & Janssen (2019)), no noise $\mathrm{d}Z_1$, and no Brownian motion $B_t^{(3)}$. Moreover, because of scaling assumption, Bôas & Young (2020) neglect the spatial diffusivity matrix, $\boldsymbol{a}$, while Smit & Janssen (2019) find $\boldsymbol{a} = 4a_0\left(\mathbb{I}_d + \frac{5}{4}\tilde{\boldsymbol{k}}\tilde{\boldsymbol{k}}^{\mathsf{T}}\right)$ (Eq. (22)-(23)). In this anisotropic framework, the Stratonovich wavevector equation (2.3), $\mathrm{d}\boldsymbol{k} = -\boldsymbol{\nabla}(\overline{\boldsymbol{v}}\mathrm{d}t + \sigma\circ\mathrm{d}B_t)^{\mathsf{T}}\boldsymbol{k}$, would involve an additional drift term in Itō notations.

Further developing this anisotropic stochastic closure is an interesting avenue. Neverthe-

less, in the present study, we adopt the isotropic model for $\sigma \mathrm{d}B_t$, which is much more convenient for multi-ray numerical simulations.

Appendix D. Jet simulation

Again, currents are simulated at a resolution 512×512 on a 1000-km-width squared domain through the same code. A backward velocity v_{Bk} forces a leftward jet structure.

$$\partial_t \omega + \boldsymbol{v} \cdot \boldsymbol{\nabla} \omega = S_\omega \quad \text{with} \quad \boldsymbol{v} = \boldsymbol{\nabla}^\perp \Delta^{-1} (\omega + \omega_{\mathrm{Bk}}). \tag{D 1}$$

S_ω encompasses the linear drag and the hyperviscosity, and the background vorticity, ω_{Bk}, is a smooth step function with a wavy interface at $y = Y_{\mathrm{Bk}}(x)$:

$$\omega_{\mathrm{Bk}}(x, y) = \Omega_{\mathrm{Bk}} \left(\tfrac{1}{2} - \mathrm{erf} \left(\frac{y - Y_{\mathrm{Bk}}(x)}{L_y^\omega} \right) \right) \text{ with } Y_{\mathrm{Bk}}(x) = L_y \left(\tfrac{1}{2} + \tfrac{1}{30} \cos \left(\tfrac{2\pi}{L_x} x \right) \right) \tag{D 2}$$

To better highlight the interplay between ray oscillations and scattering, we consider very-collimated swells, with a spatial extension of $100\lambda = 25$ km.

Besides, the curvature of the simulated jet can force an additional faster oscillation around the jet for small enough wavevector angle. Indeed, a wave group traveling exactly rightward would cross an alternation of positive and negative vorticity regions with a period $L_x/(v_g^0 - \overline{U}_0) \approx 1$ day $< 2\pi/\overline{\omega}_r$. Here, we set an initial wavevector angle large enough to prevent the additional harmonics.

REFERENCES

Bal, Guillaume & Chou, Tom 2002 Capillary–gravity wave transport over spatially random drift. *Wave Motion* **35** (2), 107–124.

Bauer, Werner, Chandramouli, Pranav, Chapron, Bertrand, Li, Long & Mémin, Etienne 2020 Deciphering the role of small-scale inhomogeneity on geophysical flow structuration: a stochastic approach. *Journal of Physical Oceanography* **50** (4), 983–1003.

Bôas, Ana B Villas & Young, William R 2020 Directional diffusion of surface gravity wave action by ocean macroturbulence. *Journal of Fluid Mechanics* **890**.

Borcea, Liliana, Garnier, Josselin & Solna, Knut 2019 Wave propagation and imaging in moving random media. *Multiscale Modeling & Simulation* **17** (1), 31–67.

Boury, Samuel, Bühler, Oliver & Shatah, Jalal 2023 Fast-slow wave transitions induced by a random mean flow. *Physical Review E* **108** (5), 055101.

Bühler, Oliver 2009 *Waves and mean flows*. Cambridge University Press.

Cotter, Colin J, Gottwald, Georg A & Holm, Darryl D 2017 Stochastic partial differential fluid equations as a diffusive limit of deterministic lagrangian multi-time dynamics. *Proceedings of the Royal Society A: Mathematical, Physical and Engineering Sciences* **473** (2205), 20170388.

Cox, Michael R, Kafiabad, Hossein A & Vanneste, Jacques 2023 Inertia-gravity-wave diffusion by geostrophic turbulence: the impact of flow time dependence. *Journal of Fluid Mechanics* **958**, A21.

Crisan, Dan & Holm, Darryl D 2018 Wave breaking for the stochastic camassa–holm equation. *Physica D: Nonlinear Phenomena* **376**, 138–143.

Dinvay, Evgueni & Mémin, Etienne 2022 Hamiltonian formulation of the stochastic surface wave problem. *Proceedings of the Royal Society A* **478** (2265), 20220050.

Dong, Wenjing, Bühler, Oliver & Smith, K Shafer 2020 Frequency diffusion of waves by unsteady flows. *Journal of Fluid Mechanics* **905**, R3.

Dysthe, Kristian B 2001 Refraction of gravity waves by weak current gradients. *Journal of Fluid Mechanics* **442**, 157–159.

Freund, JB & Fleischman, TG 2002 Ray traces through unsteady jet turbulence. *International Journal of Aeroacoustics* **1** (1), 83–96.

Garnier, Josselin, Gay, Etienne & Savin, Eric 2020 Multiscale analysis of spectral broadening of acoustic waves by a turbulent shear layer. *Multiscale Modeling & Simulation* **18** (2), 798–823.

Hell, Momme C, Fox-Kemper, Baylor & Chapron, Bertrand in preparation An efficient wave model for surface wave growth and propagation in coupled climate models. *Journal of Advances in Modeling Earth Systems* .

Heller, EJ, Kaplan, L & Dahlen, A 2008 Refraction of a gaussian seaway. *Journal of Geophysical Research: Oceans* **113** (C9).

Holm, D. 2015 Variational principles for stochastic fluid dynamics. *Proceedings of the Royal Society of London A: Mathematical, Physical and Engineering Sciences* **471** (2176).

Holm, Darryl D 2021 Stochastic variational formulations of fluid wave–current interaction. *Journal of nonlinear science* **31** (1), 4.

Holm, Darryl D, Hu, Ruiao & Street, Oliver D 2023 On the interactions between mean flows and inertial gravity waves. *arXiv preprint arXiv:2302.04838* .

Holm, Darryl D & Luesink, Erwin 2021 Stochastic wave–current interaction in thermal shallow water dynamics. *Journal of Nonlinear Science* **31**, 1–56.

Jonsson, Ivar G 1990 Wave-current interactions. *The sea* **9**, 65–120.

Kafiabad, Hossein A, Savva, Miles AC & Vanneste, Jacques 2019 Diffusion of inertia-gravity waves by geostrophic turbulence. *Journal of Fluid Mechanics* **869**, R7.

Klyatskin, V. 2005 *Stochastic equations through the eye of the physicist: Basic concepts, exact results and asymptotic approximations*. Elsevier.

Klyatskin, VI & Koshel, KV 2015 Anomalous sea surface structures as an object of statistical topography. *Physical Review E* **91** (6), 063003.

Kudryavtsev, Vladimir, Yurovskaya, Maria, Chapron, Bertrand, Collard, Fabrice & Donlon, Craig 2017 Sun glitter imagery of ocean surface waves. part 1: Directional spectrum retrieval and validation. *Journal of Geophysical Research: Oceans* **122** (2), 1369–1383.

Kunita, H. 1997 *Stochastic flows and stochastic differential equations*, , vol. 24. Cambridge university press.

Lapeyre, Guillaume 2017 Surface quasi-geostrophy. *Fluids* **2** (1), 7.

Lapeyre, G., Klein, P. & Hua, B. 1999 Does the tracer gradient vector align with the strain eigenvectors in 2D turbulence? *Physics of Fluids* **11** (12), 3729–3737.

Lavrenov, Igor 2013 *Wind-waves in oceans: dynamics and numerical simulations*. Springer Science & Business Media.

McComas, C Henry & Bretherton, Francis P 1977 Resonant interaction of oceanic internal waves. *Journal of Geophysical Research* **82** (9), 1397–1412.

Mémin, E. 2014 Fluid flow dynamics under location uncertainty. *Geophysical & Astrophysical Fluid Dynamics* **108** (2), 119–146.

Mémin, Etienne, Li, Long, Lahaye, Noé, Tissot, Gilles & Chapron, Bertrand 2022 Linear wave solutions of a stochastic shallow water model. In *Stochastic Transport in Upper Ocean Dynamics Annual Workshop*, pp. 223–245. Springer Nature Switzerland Cham.

Mikulevicius, R. & Rozovskii, B. 2004 Stochastic Navier–Stokes equations for turbulent flows. *SIAM Journal on Mathematical Analysis* **35** (5), 1250–1310.

Oksendal, B. 1998 *Stochastic differential equations*. Spinger-Verlag.

Papanicolaou, G. & Kohler, W. 1974 Asymptotic theory of mixing stochastic ordinary differential equations. *Communications on Pure and Applied Mathematics* **27** (5), 641–668.

Pierrehumbert, RT 1994 Tracer microstructure in the large-eddy dominated regime. *Chaos, Solitons & Fractals* **4** (6), 1091–1110.

Piterbarg, Leonid & Ostrovskii, A 1997 *Advection and diffusion in random media: implications for sea surface temperature anomalies*. Kluwer Academic.

Plougonven, Riwal & Zhang, Fuqing 2014 Internal gravity waves from atmospheric jets and fronts. *Reviews of Geophysics* **52** (1), 33–76.

Resseguier, Valentin, Li, Long, Jouan, Gabriel, Dérian, Pierre, Mémin, Etienne & Bertrand, Chapron 2020*a* New trends in ensemble forecast strategy: uncertainty quantification for coarse-grid computational fluid dynamics. *Archives of Computational Methods in Engineering* pp. 1–82.

Resseguier, Valentin, Mémin, Etienne & Chapron, Bertrand 2017*a* Geophysical flows under location uncertainty, part I random transport and general models. *Geophysical & Astrophysical Fluid Dynamics* **111** (3), 149–176.

Resseguier, Valentin, Mémin, Etienne & Chapron, Bertrand 2017*b* Geophysical flows under location uncertainty, part II quasi-geostrophy and efficient ensemble spreading. *Geophysical & Astrophysical Fluid Dynamics* **111** (3), 177–208.

Resseguier, Valentin, Pan, Wei & Fox-Kemper, Baylor 2020*b* Data-driven versus self-similar

parameterizations for stochastic advection by lie transport and location uncertainty. *Nonlinear Processes in Geophysics* **27** (2), 209–234.

Slunyaev, AV & Shrira, VI 2023 Extreme dynamics of wave groups on jet currents. *Physics of Fluids* **35** (12).

Smit, PB, Houghton, IA, Jordanova, K, Portwood, T, Shapiro, E, Clark, D, Sosa, M & Janssen, TT 2021 Assimilation of significant wave height from distributed ocean wave sensors. *Ocean Modelling* **159**, 101738.

Smit, Pieter B & Janssen, Tim T 2019 Swell propagation through submesoscale turbulence. *Journal of Physical Oceanography* **49** (10), 2615–2630.

Voronovich, AG 1976 Propagation of internal and surface gravity waves in the approximation of geometrical optics. *Izv. Atmos. Ocean. Phys* **12**, 850–857.

Voronovich, A. 1991 The effect of shortening of waves on random currents. In *Proceedings of nonlinear water waves*. Bristol.

Wang, Han, Bôas, Ana B Villas, Young, William R & Vanneste, Jacques 2023 Scattering of swell by currents. *arXiv preprint arXiv:2305.12163* .

West, Bruce J 1978 Ray paths in a fluctuating environment. *Physical Review A* **18** (4), 1646.

White, Benjamin S 1999 Wave action on currents with vorticity. *Journal of Fluid Mechanics* **386**, 329–344.

White, Benjamin S & Fornberg, Bengt 1998 On the chance of freak waves at sea. *Journal of fluid mechanics* **355**, 113–138.

Zhen, Yicun, Resseguier, Valentin & Chapron, Bertrand 2023 Physically constrained covariance inflation from location uncertainty. *EGUsphere* **2023**, 1.